Scientia Iranica (2024) 31(2), 149–160

SCIENTIA IRANICA

Sharif University of Technology
Scientia Iranica
Transactions D: Computer Science & Engineering and Electrical Engineering
https://scientiairanica.sharif.edu

A new hybrid analytical model based on winding function theory for analysis of unbalanced two-phase induction motors

F. Rezaee-Alam[a,*], A. Hamidi[a], and M. Hosseini[b]

a. *Departement of Electrical Engineering, Lorestan University, 68151-44316, Khorramabad, Lorestan, Iran.*
b. *Departement of Civil Engineering, Lorestan University, 68151-44316, Khorramabad, Lorestan, Iran.*

Received 31 January 2021; received in revised form 6 October 2021; accepted 18 April 2022

KEYWORDS
Air-gap;
Conformal Mapping (CM);
Hybrid Analytical Model (HAM);
Inductance;
Magnetic field;
Magnetic saturation.

Abstract. The purpose of this paper is to present a new Hybrid Analytical Model (HAM) based on Winding Function Theory (WFT) for electromagnetic analysis of the performance of one typical Unbalanced Two-Phase Induction Motor (UTPIM). Different indexes of electromagnetic modeling, such as winding distribution, slotting effect, and magnetic saturation, can be accurately considered by using the proposed HAM. To obtain this new hybrid technique, WFT is reformulated to consider magnetic saturation in addition to the influence of slotting and winding distribution. The Conformal Mappings (CMs) are used to calculate the slotted air-gap length accurately. The Magnetic Equivalent Circuit (MEC) model is used to consider the Magneto-Motive Force (MMF) drop in stator and rotor cores due to the excitation of one phase-winding. The results obtained from CMs and MEC are then utilized in reformulated WFT to calculate the inductances of the respective phase-winding. Transient analysis is then done to calculate the indexes of performance, such as air-gap magnetic field, phase currents, electromagnetic torque, and rotor speed, by using the lookup table of inductances while considering different capacitors in the auxiliary phase. In each step, the accuracy of analytical results is confirmed by comparing with corresponding results obtained from the Finite Element Method (FEM).

1. Introduction

Unbalanced Two-Phase Induction Motors (UTPIMs) are widely used in domestic appliances and low-power applications. However, due to their unbalanced structure, the performance of UTPIM is affected by the backward-rotating magnetic field. For this reason, electromagnetic modeling and analysis are necessary for the careful and thorough examination of UTPIMs with different run capacitors. Various techniques can be used for modeling and analysis of UTPIMs, such as Finite Element Method (FEM) [1,2], Winding Function Theory (WFT) [3,4], Magnetic Equivalent Circuit (MEC) [5,6], Sub-Domain (S-D) model [7,8], Conformal Mapping (CM) method [9–11], and Field Reconstruction Method (FRM) [12,13]. FEM is an accurate technique. However, FEM is a time-consuming method, and it is conventionally used to verify the analytical results in the final stage. WFT is an analytic technique to calculate the inductance matrix. However, the conventional WFT cannot consider the slotting effect and magnetic saturation. The MEC model is an accurate technique for considering the magnetic

*. *Corresponding author.*
E-mail addresses: rezaee.fa@lu.ac.ir (F. Rezaee-Alam); hamidi.a@lu.ac.ir (A. Hamidi); hosseini.m@lu.ac.ir (M. Hosseini)

doi: 10.24200/sci.2022.57654.5348

saturation in iron parts. However, the air-gap region is not accurately considered by the MEC model. In the S-D model, the motor geometry is divided into several domains for solving the Laplace or Poisson equations in each domain separately. Therefore, the computational burden of the S-D model is high. CM can be used to calculate the components of flux density in a slotted air gap. However, the conventional CM cannot consider the magnetic saturation in a ferromagnetic core. FRM acts based on applying the law of superposition on the basis of functions obtained through FEM.

According to the above explanations, the analytical techniques have some drawbacks for the analysis of electric machines. For this reason, in recent years, Hybrid Analytical Models (HAMs) have been presented, which can simultaneously consider the capabilities of different techniques for accurate modeling of electric machines [14–19]. HAM based on CM and MEC models has been used to model and analyze permanent-magnet synchronous motors in [14–17], so that the air-gap region and iron parts have been modeled by using CM and MEC, respectively. In this paper, the HAM based on WFT and MEC [18,19] is extended for electromagnetic modeling and analysis of one typical UTPIM. In reality, this HAM acts based on WFT, which is assisted by the MEC model. The main property of WFT is its easy implementation. However, the accuracy of WFT depends on the modeling accuracy of air-gap length and magnetic saturation. To this end, a virtual air-gap length function was presented in [20–22] to consider the magnetic saturation by WFT. The air-gap length function with stepped form was used in WFT while considering the slot depth of the stator and rotor [23]. It is obvious that the technique presented in [23] cannot consider the real paths of flux tubes in slotted air-gap. To solve this problem in [24,25], some FEM analysis was used to calculate the air-gap permeance while considering the effect of slots and salient poles. The effect of magnetic saturation in [23] is also considered by increasing the air-gap length under each tooth in proportion to the Magneto-Motive Force (MMF) drop in the relevant tooth. WFT has also been used to model and analyze the bearing fault by considering a suitable air-gap length function [26,27].

This paper proposes a new HAM based on WFT for transient and magnetic field analysis of one typical UTPIM, which helps from the MEC model and CMs for considering the MMF drops in iron parts and slotting effect, respectively. The organization of this paper is as follows: The proposed HAM based on WFT is introduced in Section 2. The results of the inductance matrix obtained through the proposed HAM are presented in Section 3. Transient analysis to calculate the phase currents is done in Section 4. The proposed HAM is used to calculate the air-gap magnetic field in Section 5. The conclusions of this work are presented in Section 6.

2. HAM based on WFT

WFT was first proposed in [28] for calculating the inductance matrix by following the famous formula:

$$L_{B,A} = \mu_0 r L \int_0^{2\pi} \frac{n_B(\alpha) N_A(\alpha)}{g(\alpha)} d\alpha, \tag{1}$$

where r is the radius in the middle of the air gap, L is the core length in the axial direction, α is the circumferential position in the air gap, n_A is the turn function of phase A, N_B is the winding function of phase B, $g(\alpha)$ is the distribution of air-gap length, and $L_{(A,B)}$ is the element of inductance matrix between phases A and B.

Figure 1 shows a closed path in the zoomed view of motor geometry. The ampere circuit law is written on this closed path while considering the MMF drops in iron parts as [18].

$$\oint \overrightarrow{H_A}.\overrightarrow{dl} = n_A(\alpha) I_A - n_{sat,A}(\alpha), \tag{2}$$

$$\oint \overrightarrow{H_A}.\overrightarrow{dl} = H_A(\alpha) g(\alpha) - H_A(0) g(0), \tag{3}$$

$$H_A(\alpha) = \frac{n_A(\alpha) I_A - n_{sat,A}(\alpha) + H_A(0) g(0)}{g(\alpha)}. \tag{4}$$

$n_{sat,A}(\alpha)$ represents the distribution of MMF drops enclosed in the closed path abcda due to the excitation of only phase A with I_A. $n_{sat,A}(\alpha)$ is the virtual turn function of one virtual winding with one ampere current.

Gauss's law is written on the lateral surface of one cylinder in the middle of the air gap:

$$\oint_S \mu_0 \overrightarrow{H_A(\alpha)}.\overrightarrow{dS} = 0 \rightarrow \int_0^{2\pi} H_A(\alpha) d\alpha = 0. \tag{5}$$

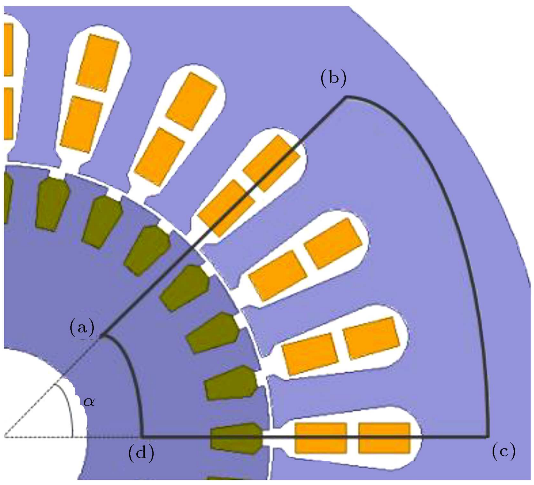

Figure 1. A zoomed view of motor geometry for applying ampere circuit law.

By replacing Eq. (4) in Eq. (5) we have:

$$H_A(0)\,g(0) = \frac{-\int_0^{2\pi} \frac{[n_A(\alpha) I_A - n_{sat,A}(\alpha)]}{g(\alpha)} d\alpha}{\int_0^{2\pi} \frac{1}{g(\alpha)} d\alpha}, \tag{6}$$

where $g(\alpha)$ is the distribution of air gap length. Then, Eq. (4) is written as:

$$H_A(\alpha) = \frac{I_A}{g(\alpha)} \left(n_A(\alpha) - \frac{\int_0^{2\pi} \frac{n_A(\alpha)}{g(\alpha)} d\alpha}{\int_0^{2\pi} \frac{1}{g(\alpha)} d\alpha} \right) - \frac{1}{g(\alpha)} \left(n_{sat,A}(\alpha) - \frac{\int_0^{2\pi} \frac{n_{sat,A}(\alpha)}{g(\alpha)} d\alpha}{\int_0^{2\pi} \frac{1}{g(\alpha)} d\alpha} \right). \tag{7}$$

"Winding function" and "virtual winding function" are defined as follows:

$$N_A(\alpha) = n_A(\alpha) - \frac{\int_0^{2\pi} \frac{n_A(\alpha)}{g(\alpha)} d\alpha}{\int_0^{2\pi} \frac{1}{g(\alpha)} d\alpha}, \tag{8}$$

$$N_{sat,A}(\alpha) = n_{sat,A}(\alpha) - \frac{\int_0^{2\pi} \frac{n_{sat,A}(\alpha)}{g(\alpha)} d\alpha}{\int_0^{2\pi} \frac{1}{g(\alpha)} d\alpha}. \tag{9}$$

The air-gap flux density and the flux linkage with phase winding B due to the excitation of only phase A are calculated as follows:

$$B_A(\alpha) = \frac{\mu_0}{g(\alpha)} \left[N_A(\alpha) I_A - N_{sat,A}(\alpha) \right], \tag{10}$$

$$\lambda_{B,A} = \mu_0 r L \int_0^{2\pi} \frac{n_B(\alpha)}{g(\alpha)} \left[N_A(\alpha) I_A - N_{sat,A}(\alpha) \right] d\alpha. \tag{11}$$

The mutual inductance between phase windings A and B is then calculated as:

$$L_{B,A} = \frac{\lambda_{B,A}}{I_A} \rightarrow L_{B,A} = \mu_0 r L \int_0^{2\pi} \frac{n_B(\alpha)}{g(\alpha)} \left[N_A(\alpha) - \frac{N_{sat,A}(\alpha)}{I_A} \right] d\alpha. \tag{12}$$

$N_{sat,A}(\alpha)$ depends on the non-linear characteristic of the ferromagnetic core and the excitation of phase $A(I_A)$. Consequently, $L_{(B,A)}$ is a non-linear function of I_A and a linear function of $n_B(\alpha)$, $N_A(\alpha)$, and $g(\alpha)$.

2.1. Calculation of air-gap length function

The flux tubes in slotted air-gap have both radial and tangential components. To calculate the magnetizing component of inductances, $g(\alpha)$ only consider the air gap length for the radial component of flux tubes. To this end, the radial component of specific complex permeance of air-gap due to stator and rotor slots is separately calculated by using CMs. The main parameters of analyzed UTPIM are shown in Table 1.

The zoomed view of air-gap geometries, including only the rotor slots, is shown in Figure 2. The following CMs are respectively used to transform the geometry in S-domain into Z-domain, W-domain, and Ψ-domain.

$$z = \log(s), \tag{13}$$

$$z = f(w) = A \int_{w_0}^{w_1} \prod_{k=1}^{n-1} (w - w_k)^{\frac{\gamma_k}{\pi} - 1} dw + C, \tag{14}$$

$$w = j \left(\log(\psi) \frac{\Delta x}{2\pi} + \frac{\Delta y}{2} - j \frac{\Delta x}{2} \right). \tag{15}$$

Table 1. Rated parameters of studied UTPIM.

Rated power	3 Hp	Rated voltage	230 V
Rated frequency	60 Hz	Number of poles	2
Air-gap length	0.52 mm	Axial length	89 mm
Stator resistance (main)	0.96 Ω	Stator resistance (auxiliary)	3.06 Ω
Number of stator slots	24	Number of rotor slots	28
The inner diameter of the stator	67.31 mm	The inner diameter of the rotor	22 mm
Stator tooth-shoe width	6.31 mm	Rotor tooth-shoe width	5.435 mm
Stator tooth-body width	4.73 mm	Rotor tooth-body width	3.33 mm
Stator slot depth	17.1 mm	Rotor slot depth	19.1 mm
Run capacitor	35 μF	Turn per coil	Variable

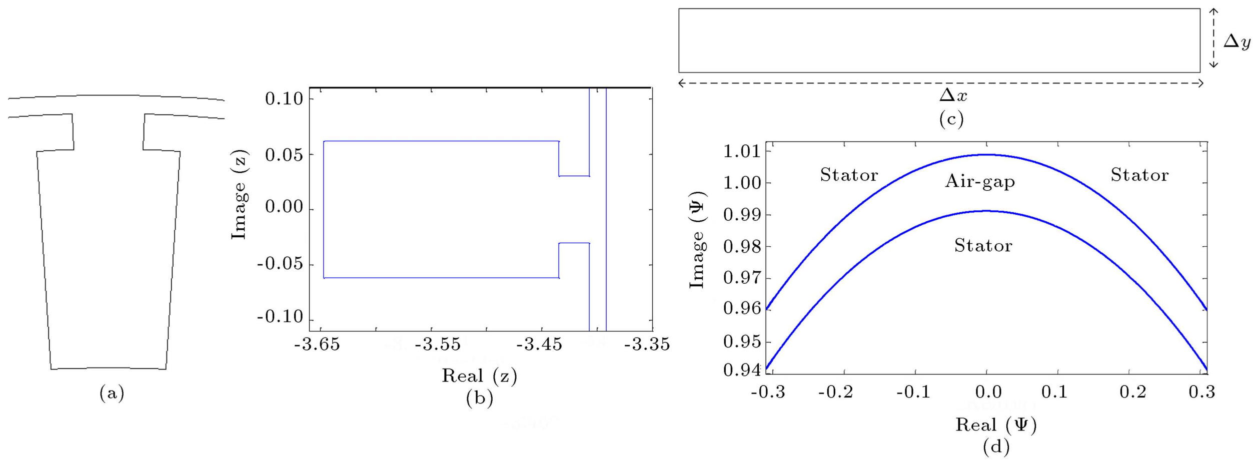

Figure 2. A zoomed view of air-gap in different domains, (a) S-domain, (b) Z-domain, (c) W-domain, and (d) Ψ-domain.

CM (14) is called the Schwarz-Christoffel (S-C) mapping, which is used to map the slotted geometry in the Z-domain into one canonical rectangle in the W-domain by using the S-C toolbox [29].

Since the air gap length of UTPIMs is small, it is sufficient that the air gap complex permeance is calculated in the middle of the air gap [19]. For this reason, one contour is considered in the middle of the air gap in the S-domain as follows:

$$S_g = R_g e^{j\alpha}, \tag{16}$$

where R_g is the radius of the contour in the air gap, and α is the angular position of a relevant point on the contour.

The corresponding contours in Z-domain, W-domain, and Ψ-domain are defined as [29]:

$$Z_g = \log\left(R_g\right) + j\alpha, \tag{17}$$

$$W_g = evalinv\left(f, Z_g\right), \tag{18}$$

$$\Psi_g = e^{-j\left(\frac{2\pi}{\Delta x}\right)\left(W_g - \frac{\Delta x}{2} - j\frac{\Delta y}{2}\right)}. \tag{19}$$

The complex permeance on this contour in the middle of the air gap (considering only the rotor slots) is calculated as:

$$\Lambda_{rotor}\left(\alpha, \theta_r\right) = \left(\frac{\partial z}{\partial s} \times \frac{\partial w}{\partial z} \times \frac{\partial \psi}{\partial w}\right)\Bigg|\; S_g, W_g, \Psi_g, \tag{20}$$

$$\frac{\partial z}{\partial s} = \frac{1}{S_g}, \tag{21}$$

$$\frac{\partial w}{\partial z} = \frac{1}{evaldiff\left(f, W_g\right)}, \tag{22}$$

$$\frac{\partial \psi}{\partial w} = -j\left(\frac{2\pi}{\Delta x}\right) e^{-j\left(\frac{2\pi}{\Delta x}\right)\left(W_g - \frac{\Delta x}{2} - j\frac{\Delta y}{2}\right)}. \tag{23}$$

The specific complex permeance of the air gap due to only the rotor slots is then calculated as:

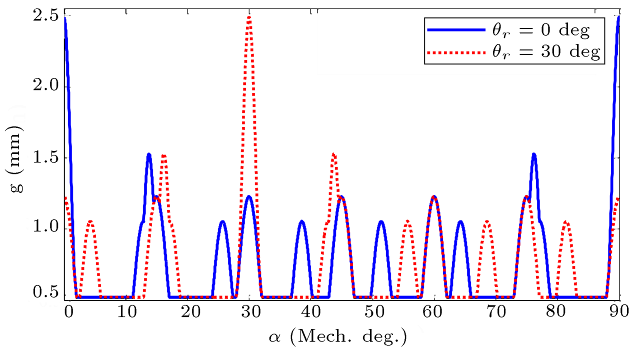

Figure 3. Distribution of slotted air-gap length.

$$\lambda_{rotor}\left(\alpha, \theta_r\right) = \frac{\Lambda_{rotor}}{\Lambda_{slotless}}\Bigg|\; S_g, W_g, \Psi_g, \tag{24}$$

where $\Lambda_{slotless}$ is the complex permeance of the slotless air gap. $\Lambda_{slotless}$ is calculated as:

$$\Lambda_{slotless} = \frac{2}{R_r + R_s}, \tag{25}$$

where R_s and R_r are, respectively, the inner radius of the stator and the outer radius of the rotor. In a similar way, the specific complex permeance of the air gap due to only the stator slots ($\lambda_{stator}(\alpha)$) can be calculated. Finally, the distribution of the slotted air gap length function is calculated as follows:

$$g\left(\alpha, \theta_r\right) = \frac{g_{slotless}}{real\left(\lambda_{stator}(\alpha)\right) \times real\left(\lambda_{rotor}\left(\alpha, \theta_r\right)\right)}, \tag{26}$$

where $g_{slotless} = R_s - R_r$.

The distribution of the slotted air gap length for two typical rotor positions is shown in Figure 3.

2.2. Calculation of $N_{sat,A}(\alpha)$

To calculate the virtual winding function, a non-linear MEC model of the analyzed UTPIM (Figure 4) should be prepared to calculate the MMF drops in different parts of the stator and rotor cores while considering

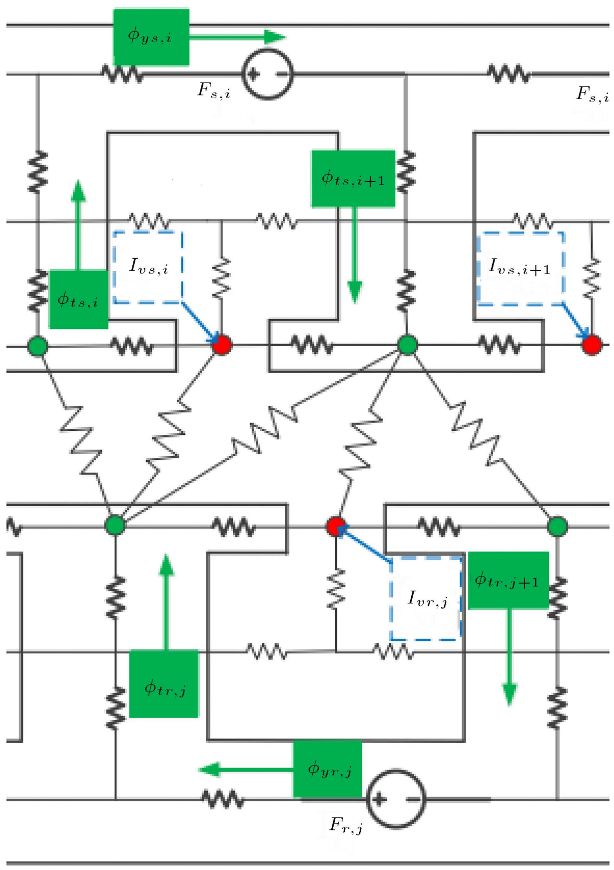

Figure 4. MEC model of analyzed UTPIM.

the relevant operating point. A non-linear algebraic equation system is obtained using the node equations for every rotor position:

$$\begin{cases} A(x)X = B \\ \mu_r = f(H) \end{cases} \tag{27}$$

where 'X' is the matrix of the scalar magnetic potential of nodes, matrix $A(x)$ depends on non-linear permeances, and matrix 'B' includes the MMF sources of the stator and rotor. The relative permeability of the core (μ_r) is a non-linear function of magnetic field intensity (H). To solve this non-linear equation system, the Newton-Raphson method has been used to calculate the matrix 'X' for every rotor position. The steps of the Newton-Raphson method are briefly presented briefly as follows:

(a) Eq. (27) is reformed as follows:

$$g(X) = A(x)X - B = 0. \tag{28}$$

(b) Non-linear equation system $g(X) = 0$ is transformed into a linear equation system by using the Jacobian matrix in iteration form (kth iteration):

$$J^k \Delta X^k = -g\left(X^k\right), \tag{29}$$

where $\Delta X^k = X^{k+1} - X^k$.

(c) The linear equation system $J^k \Delta X^k = -g\left(X^k\right)$ is solved iteratively. The iteration is terminated when the magnitude of the incremental vector $\left(\Delta X^k\right)$ becomes zero within a specified tolerance or a prespecified maximum number of iterations is reached. Here, the convergence criterion is considered as follows:

$$\left|\Delta X^k\right| \leq 0.001.$$

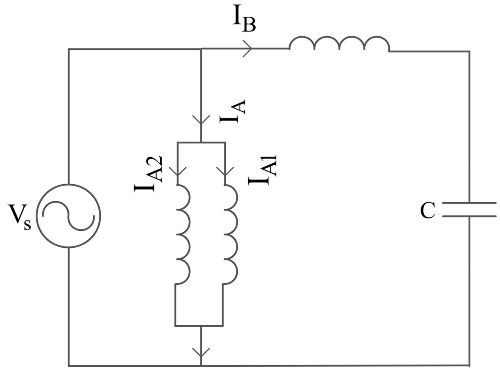

Figure 5. Stator winding circuit of analyzed UTPIM.

After obtaining the distribution of scalar magnetic potential in all nodes for relevant operating points, the magnetic flux density is also obtained in different branches. Then, the distribution of equivalent virtual currents in slot-openings of the stator and rotor is obtained as follows [18]:

$$I_{vs,i} = R_{ts,i} \times \phi_{ts,i} + R_{ys,i} \times \phi_{ys,i} + R_{ts,i+1} \times \phi_{ts,i+1}, \tag{30}$$

$$I_{vr,j} = R_{tr,j} \times \phi_{tr,j} + R_{yr,j} \times \phi_{yr,j} + R_{tr,j+1} \times \phi_{tr,j+1}, \tag{31}$$

where $R_{ts,i}$ is the reluctance of the ith tooth of the stator, $R_{ys,i}$ is the reluctance of the ith segment of the stator yoke, $R_{tr,j}$ is the reluctance of the jth tooth of the rotor, and $R_{yr,j}$ is the reluctance of the jth segment of the rotor yoke.

As shown in Figure 5, the main phase of stator winding has two parallel branches A_1 and A_2. Figure 6 shows the variation of equivalent virtual current in one typical slot (7th slot) of stator and rotor in terms of rotor positions when the branches A_1 and A_2 of the main phase are separately excited with 0.5 (A). The virtual turn function ($n_{sat,A}(\alpha'\theta_r)$) in terms of rotor positions and $\alpha = \alpha'$ can be expressed as [18]:

$$n_{sat,A}(\alpha', \theta_r) = \int_0^{\alpha'} \left[I_{vs}(\alpha, \theta_r) + I_{vr}(\alpha, \theta_r)\right] d\alpha. \tag{32}$$

The virtual winding function $N_{sat,A}(\alpha'\theta_r)$ is then calculated using Eq. (9) in terms of θ_r and $\alpha = \alpha'$.

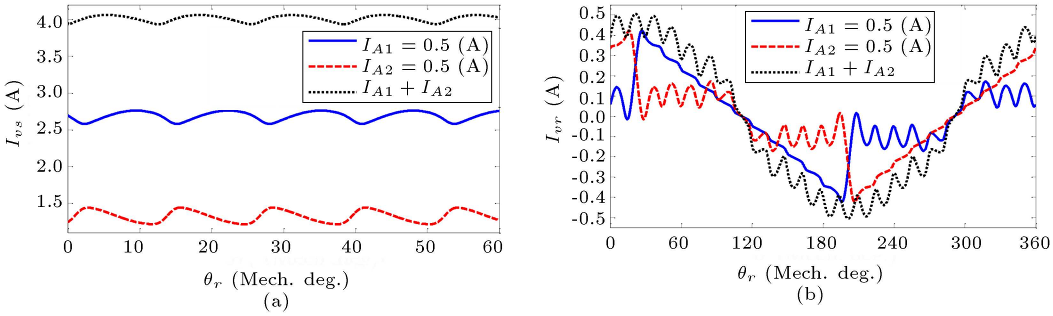

Figure 6. Magnitude of virtual currents, (a) in one stator slot and (b) in one rotor slot.

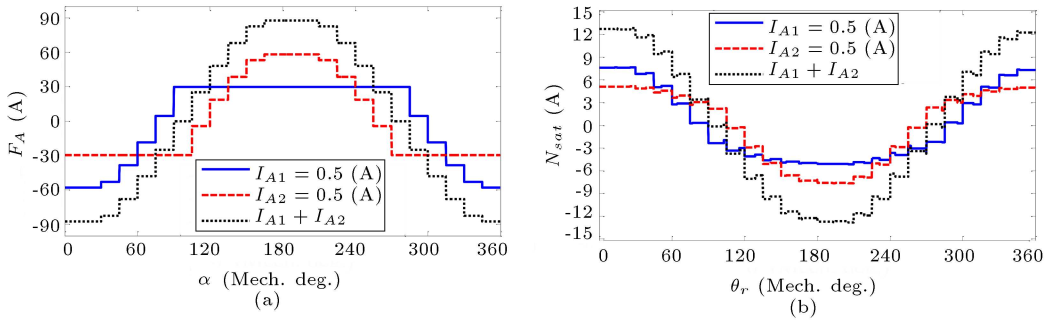

Figure 7. Winding functions of (a) Main phase of the stator, (b) Virtual winding function.

Figure 7 shows the MMF function and the virtual winding function when two branches of the main phase are separately excited with 0.5 (A). As shown in Figure 7, the MMF drop in iron parts is about 14.2% due to only the excitation of the main phase with 1 (A).

3. Inductance calculation

The proposed HAM acts based on inductance calculation for electromagnetic modeling of electric machines. To this end, the elements of the inductance matrix for this analyzed UTPIM are calculated using this HAM while considering the slotless, slotted, and saturated conditions. Table 2 and Figure 8 show some elements of the inductance matrix of studied UTPIM under slotless conditions. As seen, there is a good agreement between the corresponding results of FEM and WFT. Figure 8 also shows the elements of the mutual inductance matrix between stator phases and rotor loops, which are periodic waveforms in terms of rotor position. To calculate the inductances of phase A, each branch of the main phase is considered a separate phase. Some elements of the inductance matrix of rotor loops are shown in Figure 9, while the effect of stator and rotor slots is considered.

Table 2. Slotless inductance comparison.

Inductances	WFT	FEM
$L_{A\text{-}A}$	194.4 (mH)	192.7 (mH)
$L_{A\text{-}B}$	0 (mH)	0 (mH)
$L_{B\text{-}B}$	363 (mH)	362.2 (mH)
$L_{R1\text{-}R1}$	1.6723 (μH)	1.669 (μH)
$L_{R1\text{-}R2}$	−0.1159 (μH)	−0.1152 (μH)

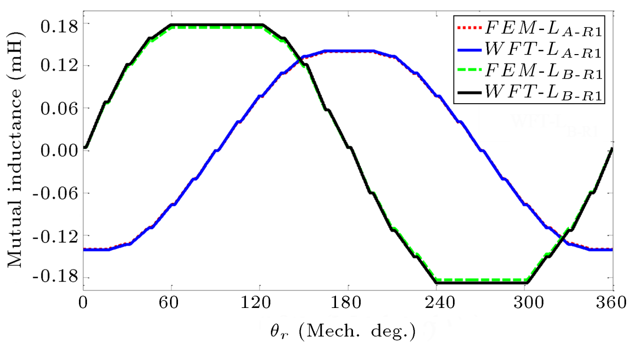

Figure 8. Slotless mutual inductance between stator and rotor.

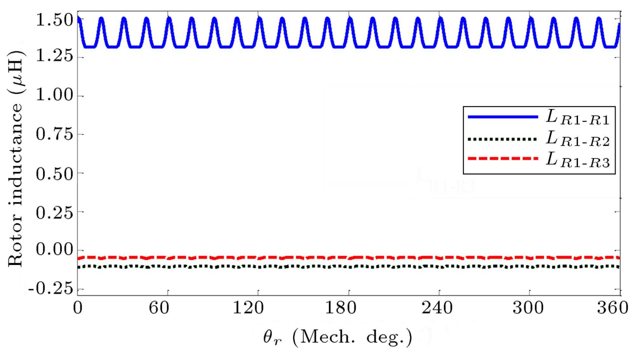

Figure 9. Slotted inductances of the rotor.

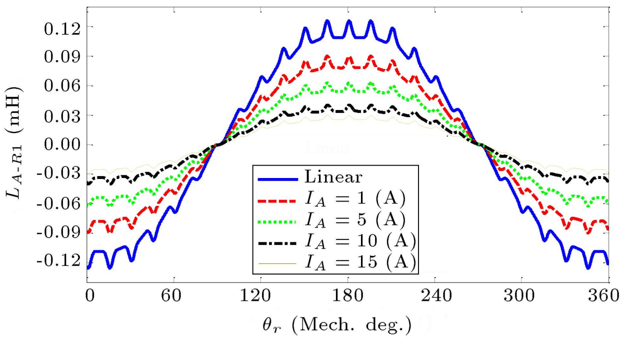

Figure 10. Mutual inductance between main phase and one rotor loop.

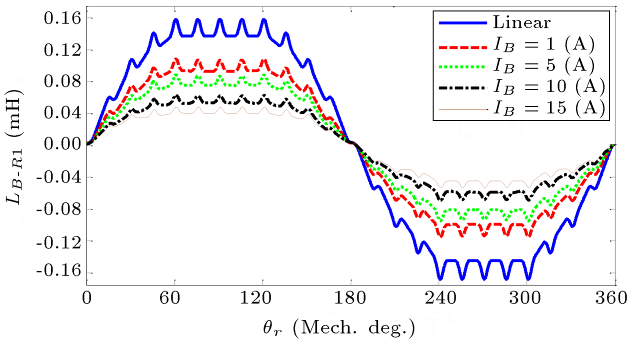

Figure 11. Mutual inductance between the auxiliary phase and one rotor loop.

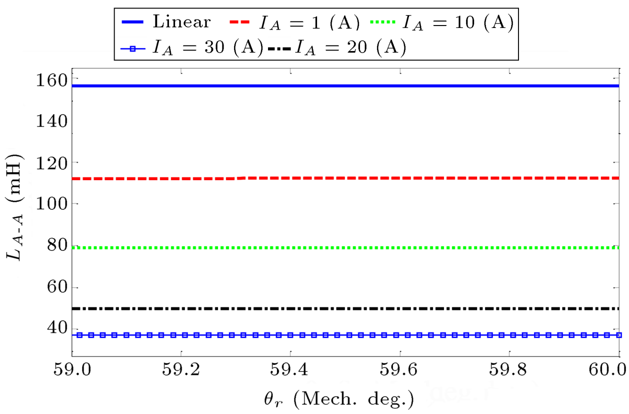

Figure 12. Self-inductance of the main phase.

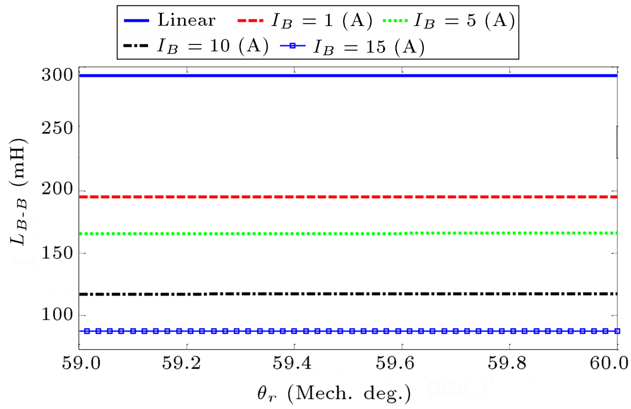

Figure 13. Self-inductance of the auxiliary phase.

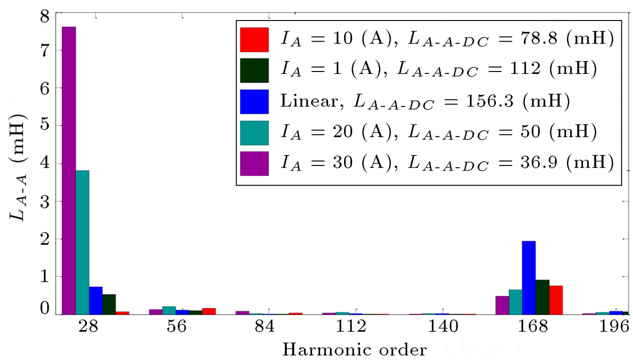

Figure 14. The harmonic content of L_{A-A}.

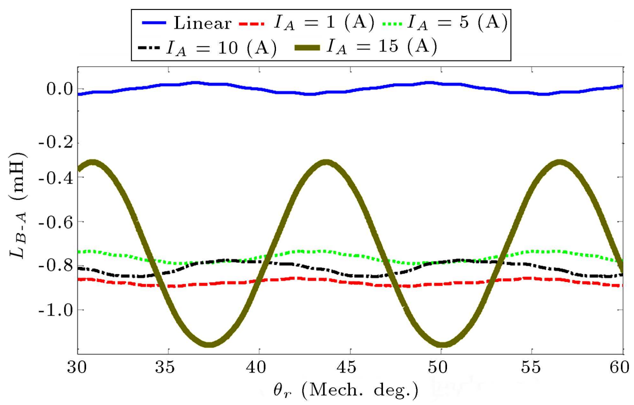

Figure 15. Mutual-inductance L_{B-A}.

The self-inductance of stator phases and the mutual inductance between stator phases and one rotor loop for different rotor positions and various excitations of relevant phases are shown in Figures 10–13 while considering the effect of slots and magnetic saturation. As shown, the DC component of self-inductances and the amplitude of the fundamental component of mutual inductances are reduced due to the effect of slots and magnetic saturation. The effect of slots on the inductances is also clearly seen.

To extract the effect of stator and rotor slots and the magnetic saturation, the harmonic component of $L_{A\text{-}A}$ is shown in Figure 14 while considering different conditions. As shown, the DC component of $L_{A\text{-}A}$ is reduced if the magnitude of I_A is increased. The 28th harmonic and its multiple are due to the rotor slot number (28 slots). The 168th harmonic is also due to the interaction effect of stator and rotor slots.

Figures 15 and 16 show the mutual inductances $L_{A\text{-}B}$ and $L_{B\text{-}A}$ between the main and auxiliary phases of the stator. As shown, $L_{A\text{-}B}$ and $L_{B\text{-}A}$ are not equal to zero when considering the slotting and magnetic saturation effects. Moreover, $L_{A\text{-}B}$ is not exactly equal to $L_{B\text{-}A}$ because the MMF distribution and, consequently, the saturation effect of the main and auxiliary phases of the stator are not the same while

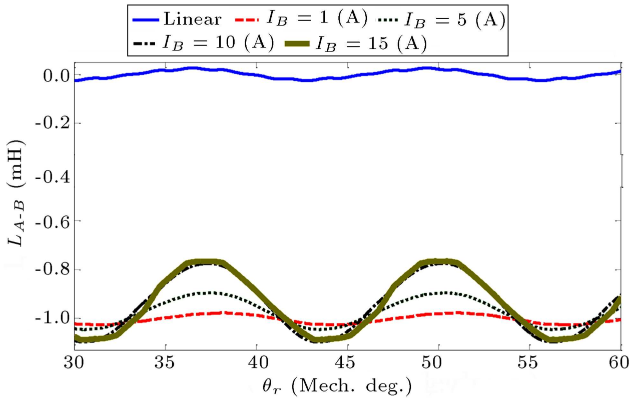

Figure 16. Mutual-inductance L_{A-B}.

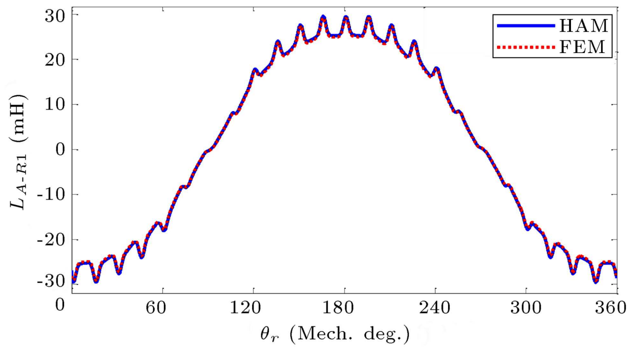

Figure 17. Validation of L_{A-R1}.

considering similar excitations of $I_A(L_{B\text{-}A})$ and I_B ($L_{A\text{-}B}$).

To confirm the accuracy of the proposed HAM for modeling the saturation and slotting effects, the corresponding results of L_{A-R1} obtained through HAM and FEM are compared in Figure 17 under the excitation $I_A = 30$ (A) and being open-circuit of other phases. As shown, there is a good agreement between results obtained through HAM and FEM.

4. Transient modeling

For transient modeling of the analyzed UTPIM, the electric circuit of the stator should be considered, as shown in Figure 5. The electric circuit of the cage-rotor is similar to the three-phase induction motors [30]. Figure 18 shows the flowchart of simulation by the proposed HAM. As explained in [30], the set of electrical and mechanical equations are defined as shown in Eq. (33). The Finite Difference Method (FDM) [31] is then used to solve the set of equations after creating a lookup table for each element of $L(\theta_r)$ and its derivative. For example, Figure 19 shows the lookup of $L_{A\text{-}A}$ as a 3-D plot in terms of the excitation I_A and the rotor position (θ_r).

The no-load transient results of analyzed UTPIM obtained through the proposed HAM are shown in Figures 20–22 when considering different run capacitors.

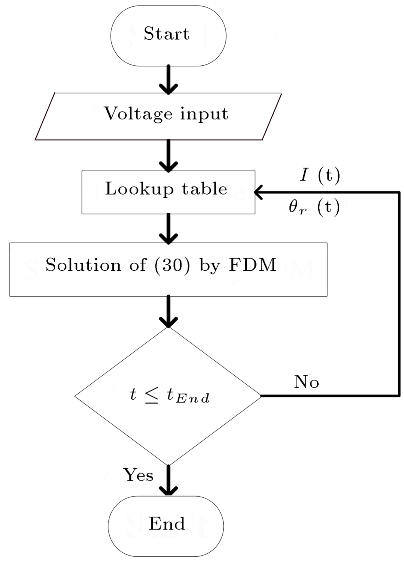

Figure 18. Flow-chart of simulation.

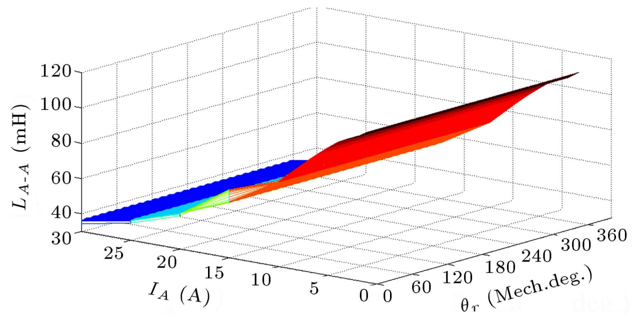

Figure 19. Lookup table of L_{A-A}.

As shown, the current amplitude of the main phase (phase A) and auxiliary phase (phase B) are respectively reduced and increased when the capacitance of the run capacitor is elevated. The total current of the stator (I_S) is the sum of I_A and I_B. The Root Mean Square (RMS) value of I_S, the input power factor of analyzed UTPIM, and the main harmonic of T_e are compared in Table 3 when considering different capacitances of the run capacitor. Figure 22 shows the analyzed UTPIM is started in a shorter time when considering $C = 45$ (μF).

$$V = R \times I + \frac{d\lambda}{dt},$$

$$\lambda = L \times I,$$

$$T_e = T_l + J\frac{d\omega_r}{dt} + D\omega_r,$$

$$W_f = \frac{1}{2}I^t \times L \times I \rightarrow T_e = \frac{\partial W_f}{\partial \theta_r},$$

$$\omega_r = \frac{d\omega_r}{dt}. \tag{33}$$

As shown in Table 3, the better performance of UTPIM

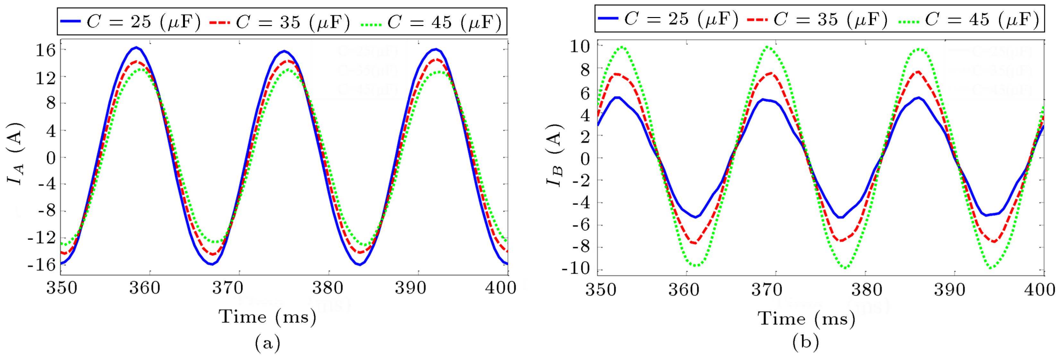

Figure 20. Stator currents of (a) main phase and (b) auxiliary phase.

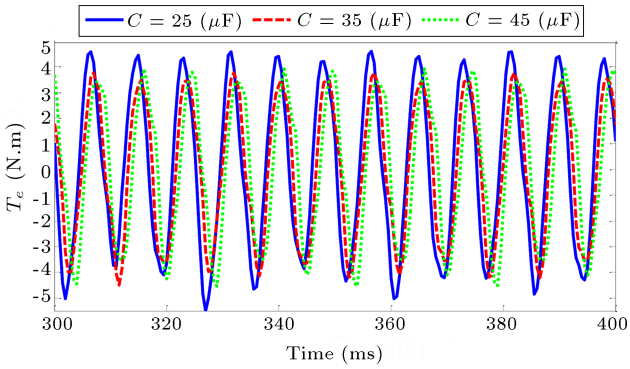

Figure 21. Electromagnetic torque.

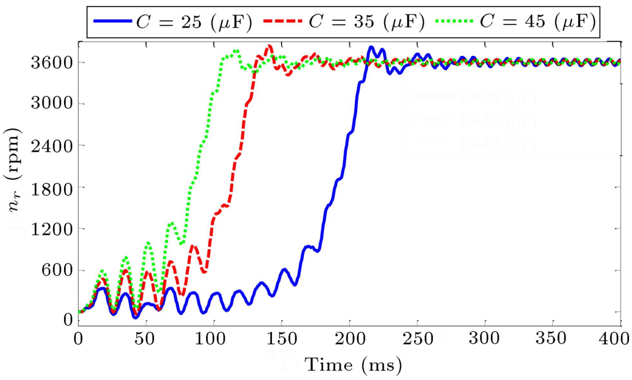

Figure 22. Rotor speed.

Table 3. Effect of run capacitor.

Capacitors	RMS value	Power factor	2nd harmonic T_e
$C = 25$ (μF)	9.66 (A)	0.43 Lag	4.56 (N.m)
$C = 35$ (μF)	8.06 (A)	0.52 Lag	3.75 (N.m)
$C = 45$ (μF)	6.8 (A)	0.68 Lag	3.95 (N.m)

is obtained by using $C = 45$ (μF). However, $C = 35$ (μF) has been selected for this analyzed UTPIM for non-technical reasons [32].

To validate the accuracy of the proposed HAM for transient modeling of analyzed UTPIM, the transient

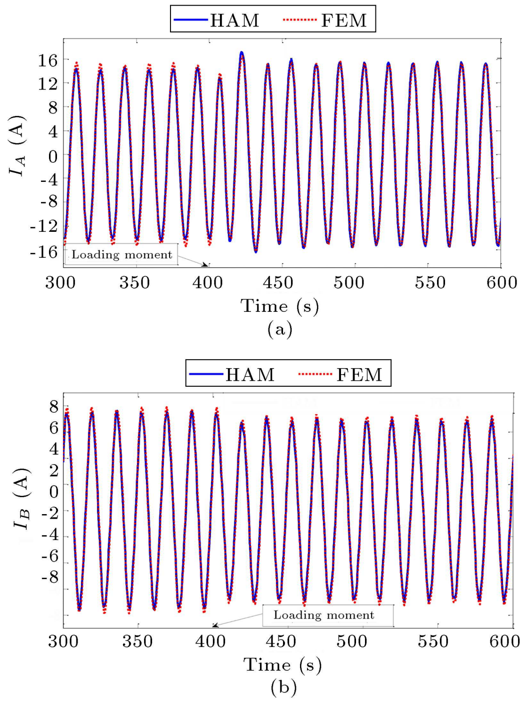

Figure 23. Validation of stator currents: (a) main phase and (b) auxiliary phase.

results obtained through HAM are compared with equivalent results obtained from FEM under no-load and loading conditions. As shown in Figures 23–25, there is a good agreement between the corresponding results of HAM and FEM. It should be noted at the moment of $t = 400$ ms, the load torque (T_L) is abruptly increased from 0 to 5 N.m.

5. Calculation of the air gap magnetic field

To calculate the air gap flux density considering all non-ideal effects, it is necessary to construct a non-linear MEC for the relevant operating point for calculating the MMF drops in teeth and yoke segments. Eqs. (30) and (31) are then used to calculate the equivalent virtual currents in the stator and rotor slots. Figure 26 shows the distribution of equivalent virtual currents in

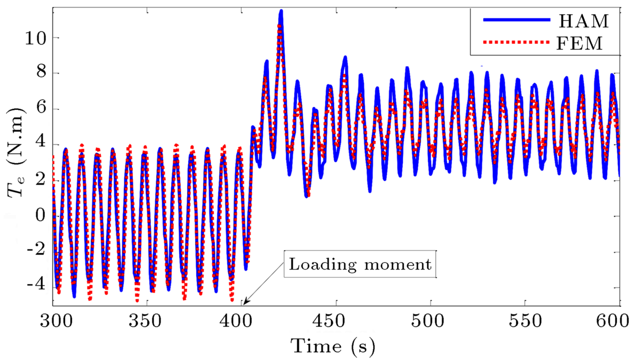

Figure 24. Validation of electromagnetic torque.

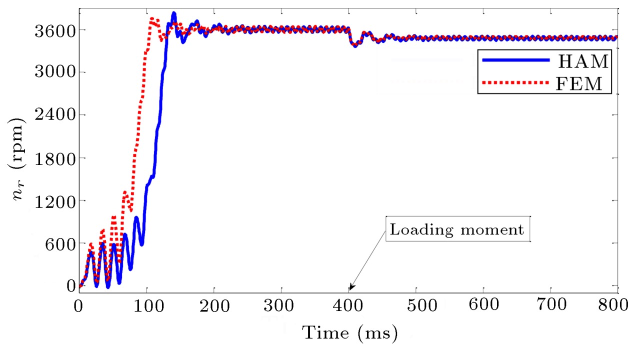

Figure 25. Validation of rotor speed.

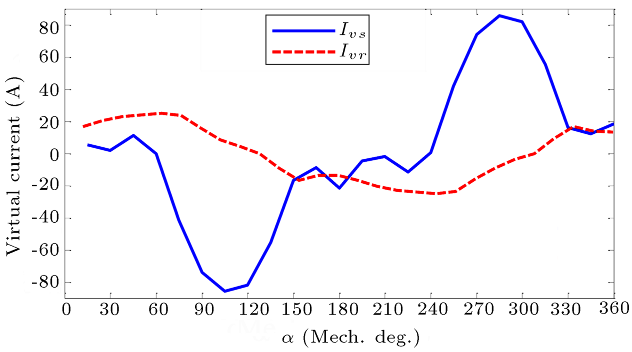

Figure 26. Distribution of equivalent virtual currents.

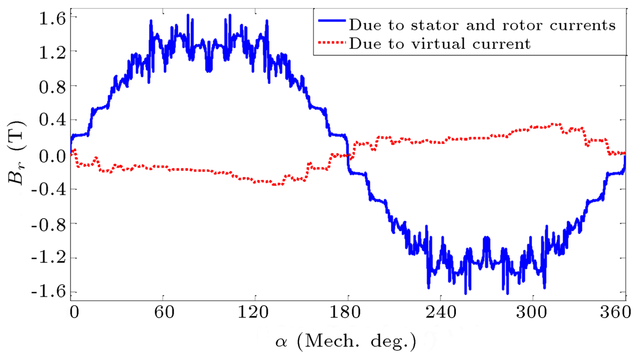

Figure 27. Distribution of real and virtual B_r.

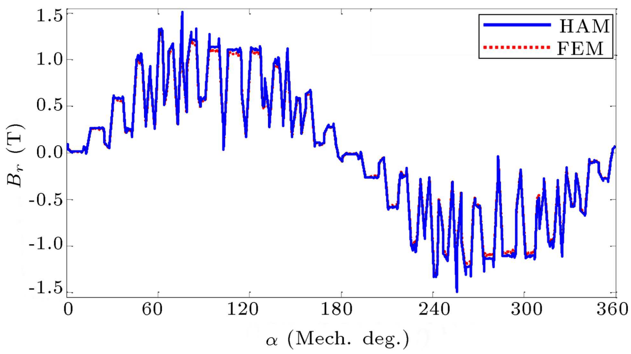

Figure 28. Saturated air-gap magnetic field.

stator and rotor slots under the steady state no-load condition.

The methods of Hague and CM [31] are then used to calculate the radial component of the slotless air gap magnetic field under the steady-state no-load condition, as shown in Figure 27.

The radial component of the saturated slotted air gap magnetic field is then calculated as follows:

$$B_r(\alpha,\theta_r) = (B_{r-sl} + B_{r-sl-v}) \times real(\Lambda_s(\alpha)) \times real(\Lambda_r(\alpha,\theta_r)), \quad (34)$$

where B_{r-sl} and B_{r-sl-v} are, respectively, caused by real and virtual currents in respective operating points. The result obtained through Eq. (34) and FEM are shown in Figure 28. As shown, there is a good agreement between B_r obtained through HAM and FEM. It should be noted that magnetic field calculation in this section has been done with $C = 35$ (μF).

The influence of different run capacitors on the magnitude and rotation speed of the fundamental component of the air gap rotating magnetic field is also studied. As shown in Figure 29 and Table 4, the best results are obtained using C=35 (μF) and C=45 (μF) as the run capacitors.

6. Conclusion

In this paper, a new Hybrid Analytical Model (HAM) based on Winding Function Theory (WFT), Magnetic Equivalent Circuit (MEC), and Conformal Mappings (CMs) was introduced, which can accurately consider non-ideal effects, including the effects of stator and rotor slots, magnetic saturation, and winding distribution. The specific complex permeance of the air gap due to the stator and rotor slots was separately calculated through CMs to consider the effect of real paths of flux tubes in slotted air-gap length. The distribution of equivalent virtual currents in the stator and rotor slots is used to consider the effect of the ferromagnetic core. As shown, different elements of the inductance matrix were predicted very well using the proposed HAM. The inductance results also show the effect of magnetic saturation on inductance reduction can be more pronounced than the slotting effect. To

Table 4. Effect of run capacitors on rotating magnetic field.

Capacitors	Ripple of $\|B_1\|$	Mean value of $\|B_1\|$	Ripple of n_s	Mean value of n_s
$C = 25$ (μF)	0.0352 (T)	0.9317 (T)	241.16 (rpm)	3588.7 (rpm)
$C = 35$ (μF)	0.0283 (T)	0.949 (T)	172.7 (rpm)	3591.5 (rpm)
$C = 45$ (μF)	0.0282 (T)	0.967 (T)	185.7 (rpm)	3599.9 (rpm)

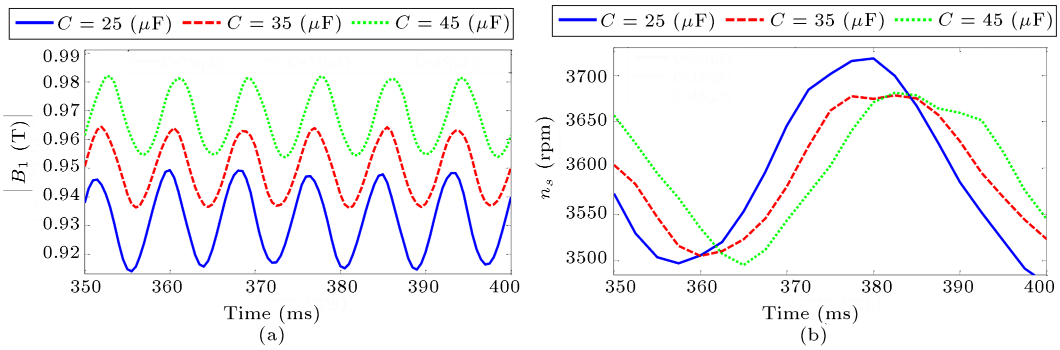

Figure 29. Amplitude and speed of rotating magnetic field.

perform the transient analysis in a short time considering different run capacitors, a 3-D lookup table for each element of the inductance matrix and its derivative was prepared in advance. It can be concluded that there are no restrictions for the electromagnetic modeling of different electric machines by the proposed HAM.

References

1. Saneie, H., Daniar, A., and Nasiri-Gheidari, Z. "Design optimization of a low speed small scale modular axial flux permanent magnet synchronous generator for urban wind turbine application", *Sci. Iran.*, **96**(6), pp. 3326–3337 (2022).

2. Sharma, U. and Singh, B. "Robust design methodology for single phase induction motor ceiling fan", *IET Electr. Power Appl.*, **14**(10), pp. 1846–1855 (2020).

3. Ojaghi, M. and Mohammadi, M. "Unified modeling technique for axially uniform and nonuniform eccentricity faults in three-phase squirrel cage induction motors", *IEEE Trans. Ind. Electron.*, **65**(7), pp. 5292–5301 (2018).

4. Alipour-Sarabi, R., Nasiri-Gheidari, Z., Tootoonchian, F., et al. "Improved winding proposal for wound rotor resolver using genetic algorithm and winding function approach", *IEEE Trans. Ind. Electron.*, **66**(2), pp. 1325–1334 (2019).

5. Naderi, P., Sharouni, S., and Moradzadeh, M. "Analysis of partitioned stator flux-switching permanent magnet machine by magnetic equivalent circuit", *Int. J. Electr. Power Energy Syst.*, **111**, pp. 369–381 (2019).

6. Saneie, H. and Nasiri-Gheidari, Z. "Performance analysis of outer-rotor single-phase induction motor based on magnetic equivalent circuit (MEC)", *IEEE Trans. Ind. Electron.*, **68**(2), pp. 1046–1054 (2021).

7. Zhang, Z., Xia, C., Yan, Y., et al. "A hybrid analytical model for open-circuit field calculation of multilayer interior permanent magnet machines", *J. Magn. Magn. Mater.*, **435**, pp. 136–145 (2017).

8. Wu, L., Zhu, M., Wang, D., et al. "A subdomain model for open-circuit field prediction in dual-stator consequent-pole permanent magnet machines", *IEEE Trans. Magn.*, **55**(8), Article Sequence Number: 8204212 (2019).

9. Min, S.G. and Sarlioglu, B. "Analytical prediction and multi constrained nonlinear optimization of slotted linear PM motors taking into account two-dimensional end effects", *IEEE Trans. Ind. Electron.*, **67**(4), pp. 2965–2976 (2020).

10. Zhou, Y. and Xue, Z.Q. "Analytical method for calculating the magnetic field of spoke-type permanent-magnet machines accounting for eccentric magnetic pole", *IEEE Trans. Ind. Electron.*, **68**(3), pp. 2096–2107 (2021).

11. Guo, B., Huang, Y., Peng, F., et al. "A new hybrid method for magnetic field calculation in IPMSM accounting for any rotor configuration", *IEEE Trans. Ind. Electron.*, **66**(7), pp. 5015–5024 (2019).

12. Torregrossa, D., Fahimi, B., Peyraut, F., et al. "Fast computation of electromagnetic vibrations in electrical machines via field reconstruction method and knowledge of mechanical impulse response", *IEEE Trans. Ind. Electron.*, **59**(2), pp. 839–847 (2012).

13. Guo, R., Yu, H., and Guo, B. "Analysis of a tubular linear permanent magnet oscillator with auxiliary teeth configuration for energy conversion system", *IEEE Trans. Transp. Electrif.*, **6**(2), pp. 602–611 (2020).

14. Farhadian, M., Moallem, M., and Fahimi, B. "Analytical calculation of magnetic field components in synchronous reluctance machine accounting for rotor

flux barriers using combined conformal mapping and magnetic equivalent circuit methods", *J. Magn. Magn. Mater.*, **505**, 166762 (2020).

15. Wu, L.J., Li, Z., Wang, D., et al. "On-load field prediction of surface-mounted PM machines considering nonlinearity based on hybrid field model", *IEEE Trans. Magn.*, **55**(3), Article Sequence Number: 8100911 (2019).

16. Li, Z., Huang, X., Wu, L., et al. "Open-circuit field prediction of interior permanent-magnet motor using hybrid field model accounting for saturation", *IEEE Trans. Magn.*, **55**(7), Article Sequence Number: 8100911 (2019).

17. Li, Z., Huang, X., Wu, L., et al. "An improved hybrid field model for calculating on-load performance of interior permanent-magnet motors", *IEEE Trans. Ind. Electron.*, **68**(10), pp. 9207–9217 (2021).

18. Rezaee-Alam, F. and Rezaeealam, B. "An enhanced analytical technique based on winding function theory for analysis of induction motors", *Int. Trans. on Electr. Energy Syst.*, **31**(5), e12863 (2021).

19. Rezaee-Alam, F., Rezaeealam, B., and Naeini, V. "An improved winding function theory for accurate modeling of small and large air-gap electric machines", *IEEE Trans. Magn.*, **57**(5), Article Sequence Number: 8104513 (2021).

20. Nandi, S. "A detailed model of induction machines with saturation extendable for fault analysis", *IEEE Trans. Ind. Appl.*, **40**(5), pp. 1302–1309 (2004).

21. Tu, X., Dessaint, L., Champagne, R., et al. "Transient modeling of squirrel-cage induction machine considering air-gap flux saturation harmonics", *IEEE Trans. Ind. Electron.*, **55**(7), pp. 2798–2809 (2008).

22. Ghoggal, A. and Hamida, A.H. "Transient and steady-state modeling of healthy and eccentric induction motors considering the main and third harmonic saturation factors", *IET Electr. Power Appl.*, **13**(7), pp. 901–913 (2019).

23. Ojaghi, M. and Nasiri, S. "Modeling eccentric squirrel-cage induction motors with slotting effect and saturable teeth reluctances", *IEEE Trans. Energy Conver.*, **29**(3), pp. 619–627 (2014).

24. Tessarolo, A. "Accurate computation of multiphase synchronous machine inductances based on winding function theory", *IEEE Trans. Energy Conver.*, **27**(4), pp. 895–904 (2012).

25. Saied S.A., Abbaszadeh, K., Tenconi, A., et al. "New approach to cogging torque simulation using numerical functions", *IEEE Trans. Ind. Appl.*, **50**(4), pp. 2420–2426 (2014).

26. Ojaghi, M. and Akhondi, R. "Modeling induction motors under mixed radial-axial asymmetry of the air gap produced by oil-whirl fault in a sleeve bearing", *IEEE Trans. Magn.*, **54**(11), Article Sequence Number: 8205105 (2018).

27. Ojaghi, M., Sabouri, M., and Faiz, J. "Analytic model for induction motors under localized bearing faults", *IEEE Trans. Energy Conver.*, **33**(2), pp. 617–626 (2018).

28. Shmitz, N.L. and Novotny, D.W., *Introductory Electromechanics*, New York: Roland (1965).

29. Driscoll, T.A. and Trefethen, L.N., *Schwarz-Christoffel Mapping*, Cambridge University Press (2002).

30. Toliyat, H.A., Arefeen, M.S., and Parlos, A.G. "A method for dynamic simulation of Air-gap eccentricity in induction machines", *IEEE Trans. Ind. Appl.*, **32**(4), pp. 910–918 (1996).

31. Rezaeealam, B. and Rezaee-Alam, F. "A new optimal design of surface mounted permanent magnet synchronous motors with integral slot per pole", *Int. J. Com. Mat. (COMPEL)*, **37**(1), pp. 136–152 (2018).

32. Maxwell 14. Documentation Center; 2010. http://www.Ansoft.com.

Biographies

Farhad Rezaee-Alam received a BSc degree from Shahid Chamran University of Ahwaz, Ahwaz, Iran, in 2007 and MSc and PhD degrees from Khajeh Nasir University of Technology, Tehran, Iran, in 2010 and 2015, respectively, all in Electrical Engineering. He is currently an Assistant Professor in the Department of Electrical Engineering at Lorestan University, Iran. His research interests include the design and modeling of electric machines.

Abdolsamad Hamidi received a PhD in Electrical Engineering from Razi University of Kermanshah, Iran in 2018. He is currently an Assistant Professor in the Department of Electrical Engineering at Lorestan University, Iran. His research interests include the design, modeling, and control of power electronic converters.

Mojtaba Hosseini is currently an Associate Professor of Structural Engineering at Lorestan University, Khorramabad, Lorestan, Iran. His research interests include analysis of structures, dynamics of structures, finite element analysis, and stability theory of structures.